ACSNANO

www.acsnano.org

ARTICLE

Multimode Interference of Bloch Surface Electromagnetic Waves

Kirill R. Safronov, Dmitry N. Gulkin, Ilya M. Antropov, Ksenia A. Abrashitova, Vladimir O. Bessonov,* and Andrey A. Fedyanin

Cite This: *ACS Nano* 2020, 14, 10428−10437

Read Online

ACCESS | Metrics & More | Article Recommendations | Supporting Information

ABSTRACT: **Integrated photonics aims at on-chip controlling light in the micro- and nanoscale ranges utilizing the waveguide circuits, which include such basic elements as splitters, multiplexers, and phase shifters. Several photonic platforms, including the well-developed silicon-on-insulator and surface-plasmon polaritons ones, operate well mostly in the IR region. However, operating in the visible region is challenging because of the drawbacks originating from absorption or sophisticated fabrication technology. Recently, a new promising all-dielectric platform based on Bloch surface electromagnetic waves (BSWs) in multilayer structures and functioning in the visible range has emerged finding a lot of applications primarily in sensing. Here, we show the effect of multimode interference (MMI) of BSWs and propose a method for implementing the advanced integrated photonic devices on the BSW platform. We determine the main parameters of MMI effect and demonstrate the operation of Mach−Zehnder interferometers with a predefined phase shift proving the principle of MMI BSW-based photonics in the visible spectrum. Our research will be useful for further developing a versatile toolbox of the BSW platform devices which can be essential in integrated photonics, lab-on-chip, and sensing applications.**

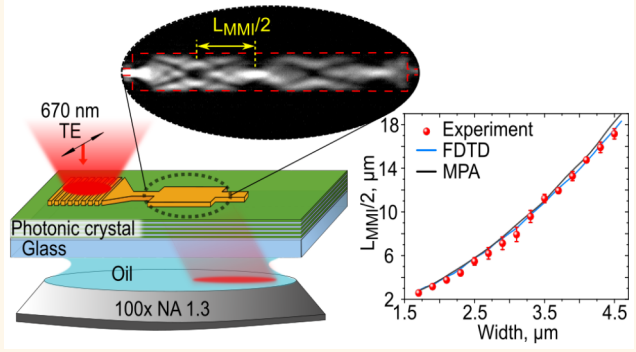

KEYWORDS: *Bloch surface waves, integrated photonics, photonic crystals, multimode interference devices, waveguide couplers, Mach−Zehnder interferometer*

Photonic integrated circuits consisting of waveguides, splitters, interferometers, multiplexers, *etc.* are the key elements for implementing all-optical computing and low-loss data transfer using both classical[1] and quantum[2] light. The common approach of implementing the waveguide regime relies on creating a refractive index contrast when the light is captured in a medium with a higher refractive index. The waveguide miniaturization requires a high refractive index contrast, so the waveguide core and cladding should be made of different materials that are compatible with each other and capable of being structured. This limits the possible combinations of materials and imposes the need to use sophisticated multistage fabrication techniques to develop integrated optical platforms, especially those operating in the visible range.[3] Another approach to on-chip controlling light is to use two-dimensional surface electromagnetic waves (SEW) propagating along an interface between two media. The waveguide regime can be obtained by structuring one of the media, which is widely demonstrated for surface plasmons,[4] and more recently for Tamm plasmons[5] and Dyakonov surface waves.[6] The possibility of applying the low-refractive-index materials,[7] such as polymers, which are easily structured using industrial lithography techniques, makes SEW approach highly promising for integrated photonics. However, the use of metals is always accompanied by ohmic losses dramatically increasing in the visible range, while the use of anisotropic materials significantly limits the propagation direction of Dyakonov waves. This leads to the quest for alternative photonic platforms that do not suffer from these limitations.

At this moment, a promising all-dielectric 2D photonic platform based on Bloch surface waves (BSWs) is being actively developed. BSWs are surface electromagnetic waves that exist at the interface between a truncated periodic dielectric multilayer (1D photonic crystal (PC)) and an

Received: May 22, 2020
Accepted: July 27, 2020
Published: July 27, 2020

https://dx.doi.org/10.1021/acsnano.0c04301
ACS Nano 2020, 14, 10428−10437

adjacent dielectric medium.[8] BSWs are sustained in the spectral region of the PC photonic stopband and outside the light cone. The frequencies and values of the wavevectors of TM- and TE-polarized BSWs are fully controlled by the structure and parameters of the PC[9] resulting in great freedom in the choice of PCs materials (including CMOS-compatible[10]) in designing the BSW platform. BSWs were demonstrated in the ultrawide range of excitation frequencies from UV[11] to C-band[12] and mid-IR[13] region. The use of lossless dielectric media guarantees a long propagation length up to several millimeters[14] and even up to centimeters[15] in the visible. All these attractive features have inspired various studies aiming at application of BSWs primarily in sensors[16,17] as well as for micromanipulation,[18] surface-enhanced Raman scattering,[19] and exciton-polariton excitation.[20,21] The BSW-induced effects such as giant Goos−Hanchen shift,[22] enhanced magneto-optical[23] and nonlinear optical[24] effects, and enhanced fluorescence emission[25] were also observed. The combination of planar nature, spectral flexibility, large propagation length and field enhancement of up to 4 orders of magnitude[26] makes BSW platform highly promising for integrated optical technologies.

The first step in developing BSW integrated optic platform is gaining control of BSW propagation. As in the case of other types of surface waves, this can be achieved by simply structuring the top layer of the PC[27] or a thin dielectric layer deposited on top of the PC.[28] This concept is widely used to control BSWs on a bare surface of the PC, particularly to generate,[29−31] split,[32] and focus[33,34] BSWs. The BSW waveguide modes were first observed in a thin polymer ridge on the surface of the PC.[35] Subsequently, only a few BSW waveguide configurations were studied, including straight[36,37] and curved[38] waveguides, disk[39] and ring[40] resonators.

In this work, we expand the concept of BSW-based integrated photonics and develop an approach to implement the integrated optical splitters and phase shifters using multimode interference (MMI) effect. The operation of MMI devices is based on the self-image principle, which manifests itself in multimode waveguides as periodic reproduction of the input field profile in one or multiple replicas (self-images) due to the interference of a number of waveguide modes.[41] MMI devices are fundamental elements in advanced photonic circuits[2] and are widely applied for on-chip splitting,[42] multiplexing,[43] and switching[44] due to their compactness, low losses, large fabrication tolerance,[45] and large optical bandwidth.[46] We prove both experimentally and numerically the multimode interference of Bloch surface waves propagating inside polymer multimode waveguides fabricated on top of a one-dimensional photonic crystal. We visualize the MMI patterns using leakage radiation microscopy, study their properties depending on the width of the waveguides, and develop MMI couplers and phase shifters on the BSW platform. Based on the obtained results, we have successfully designed and fabricated Mach−Zender interferometers (MZI) with the phase shift of 0 and π, showing constructive and destructive interference at the output port.

RESULTS

Sample Design and Experimental Technique. The studied system and the experimental idea behind it are illustrated in Figure 1a. The sample is a one-dimensional PC with polymer waveguide structure on its surface. The most important parameter of the waveguide is its height, which

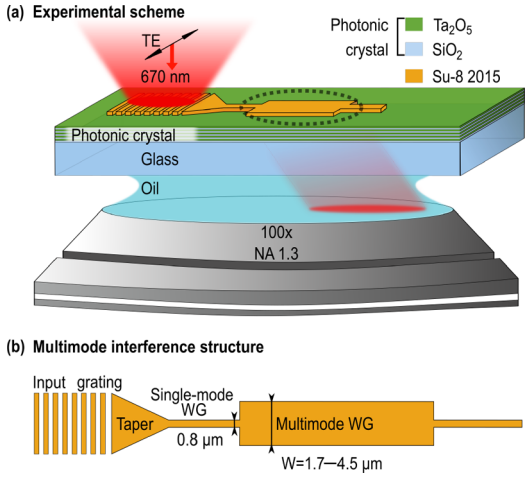

Figure 1. Sample design and experimental idea. (a) Schematic of 1D photonic crystal with polymer waveguide structure sustaining Bloch surface wave multimode interference and experimental idea of leakage radiation microscopy. Laser radiation with the wavelength of 670 nm is focused into the coupling grating and excites Bloch surface waves propagating inside the polymer waveguide. Multimode interference pattern formed by guided Bloch surface wave modes and leaked through the substrate is collected from the circled area using an oil-immersion objective lens. (b) Schematic representation of a multimode interference structure on the photonic crystal surface. All of the elements have the same height of 210 nm.

determines the maximum effective refractive index of BSW waveguide modes. The height can vary from tens to hundreds of nanometers depending on the PC parameters. Herein, we chose the PC consisting of five pairs of SiO_2/Ta_2O_5 quarter-wavelength-thick alternating layers sputtered on a coverslip. The thicknesses of layers are 140 nm (SiO_2) and 98 nm (Ta_2O_5), which correspond to the Bragg wavelength of λ_B = 810 nm. The PC topmost layer is the Ta_2O_5 layer with a higher refractive index. In this case, the BSWs cannot exist on a bare surface of PC, and their excitation requires an additional dielectric layer.[9] Thus, a 210 nm thick layer of SU-8 photoresist was spin-coated on top of PC and structured by two-photon laser lithography technique[36] to obtain a series of coupling and waveguide elements sustaining BSW excitation and propagation. The height of all fabricated elements was governed by the height of the SU-8 film and amounted to 210 nm providing the BSW waveguide modes with the maximum value of effective refractive index of $n_{\mathrm{eff}}^{\mathrm{max}}$ = 1.13 for TE-polarized excitation radiation with the wavelength of 670 nm. A detailed description of the photonic crystal properties and fabrication of polymer structures are reported in ref 36 and described in the Methods and in the Supporting Information, Section S1.

Figure 1b schematizes the structure designed to study the multimode interference of BSW. The MMI structures consist of a coupling part composed of diffraction grating with a focusing taper and a waveguide part containing an input narrow single-mode waveguide followed by a wide multimode waveguide terminated by an output single-mode waveguide. The fundamental BSW mode propagating in the input single-mode waveguide excites a set of BSW modes in the multimode waveguide. The modes interfere with each other and form a periodic pattern of field distribution (self-images) within the multimode waveguide. The number of interfering modes and

https://dx.doi.org/10.1021/acsnano.0c04301
ACS Nano 2020, 14, 10428−10437

their effective refractive indices determine the number and spatial distribution of self-images and strongly depend on the width of the multimode waveguide. Thus, we fabricated a series of MMI structures with different multimode waveguide widths from 1.7 to 4.5 μm corresponding to the excitation of the $TE_{02} - TE_{06}$ highest order mode. The width of the single-mode waveguide was equal to 0.8 μm that allows only the TE_{00} BSW mode to exist inside the waveguide (see Supporting Information, Section S2). The lengths of single-mode and multimode waveguides were fixed to 15 and 46 μm, respectively. The grating period was chosen to be 1340 nm to couple the radiation of the 670 nm laser diode with BSW *via* the second diffraction order.

The effect of multimode interference of BSWs was studied using leakage radiation microscopy (LRM) technique.[27,47,48] The scheme of the experiment is shown in Figure 1a. A collimated beam of 670 nm laser diode was focused by an objective lens (NA = 0.2) into the input grating of the MMI structure at the normal incidence. The radiation polarization was parallel to the bars of the diffraction grating to obtain TE-polarized light in the second diffraction order. Since the double reciprocal grating vector is equal to the wavenumber k_0 of the incident light, the wave vectors β of BSWs excited by the grating are varied from k_0 to 1.2 k_0. Thus, the proposed coupling scheme allows one to excite a waveguide mode with the maximum value of effective refractive index $n_{eff} = \beta/k_0 = 1.2$ which is larger than the maximum value $n_{eff}^{max} = 1.13$ of BSW modes that can occur in MMI structures under study. As a result, in the experiment, BSW modes are always excited by the grating inside the taper which focuses them into the single mode waveguide. Due to the sufficiently large length of the single mode waveguide, only the fundamental TE_{00} BSW mode reaches the multimode waveguide and initiates the multimode interference.

As BSWs propagate within the waveguides, some part of the radiation leaks into the substrate at angles θ corresponding to the condition of $\beta = n_{sb}k_0 \sin(\theta)$, where $n_{sb} = 1.52$ is the refractive index of the substrate. The intensity of leakage radiation is proportional to the near-field intensity of BSWs.[49] Hence, the evanescent electric field distribution of BSWs inside the MMI structure can be visualized by imaging the spatial intensity distribution of leakage radiation. The imaging system was based on oil-immersion objective lens with a high numerical aperture (NA = 1.3) allowing us to collect the leakage radiation of BSW waveguide modes with $n_{eff} \leq 1.3$. The collected light was spatially filtered to block the unwanted radiation passing through or scattered on the diffraction grating. The image of the sample formed by leakage radiation was built on the sensor of CMOS camera. A detailed description of LRM setup is given in the Materials and in the Supporting Information, Section S3.

Multimode Interference. Figure 2a shows the atomic force microscopy (AFM) image of a typical MMI structure and Figure 2b depicts a cross-sectional view of the wide multimode waveguide. The waveguide has a rectangular shape in the cross-section and its height is 210 ± 5 nm. A slight slope of the waveguide walls is most likely related to the finite size of the AFM probe, and the width of the waveguides was determined by the width of its top part. The LRM image of the MMI structure with 3.3 μm wide multimode waveguide is presented in Figure 2c. Propagating BSW shows behavior typical of MMI of waveguide modes: LRM image is a periodical pattern of intensity maxima. The bright spots correspond to self-images

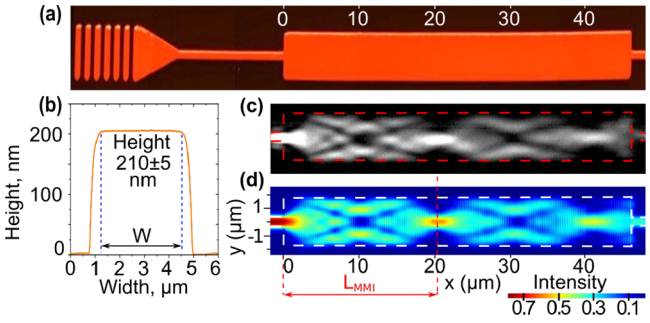

Figure 2. Multimode interference of Bloch surface electromagnetic waves. (a) AFM image of a typical MMI structure fabricated on top of a photonic crystal. (b) Cross-sectional AFM view of the multimode waveguide with W = 3.3 μm. The edges by which the waveguide width is determined are marked by vertical dotted lines. (c, d) Experimental image of the leakage radiation collected from MMI structure with W = 3.3 μm and corresponding near-field distribution calculated by FDTD method for the waveguide structure of the same geometrical parameters.

of the input field distribution. The number of self-images in the waveguide cross-section periodically varies along the waveguide. Figure 2d shows the result of numerical calculations of near-field distribution within the MMI structure with experimental geometrical parameters. The periodic pattern of BSW near-field intensity perfectly coincides with the experimental LRM image. The details of numerical calculations are provided in the Methods.

We define MMI period L_{MMI} as a longitudinal distance from the beginning of the multimode waveguide to the first single self-image or as the distance between two single self-images. For the system shown in Figure 2, L_{MMI} is approximately 20 μm. The first N-fold image is located at the distance of L_{MMI}/N from the input edge of the waveguide and can be used to implement $1 \times N$ splitting. The maximum N value is determined by the number of the highest order waveguide mode that can be sustained by the multimode waveguide and depends on its width. For example, to create a simple 1×2 MMI coupler we set the length of the multimode waveguide to $L_{MMI}/2$ and aligned the centers of the output waveguides to the positions of the BSW intensity maxima in the 2-fold image (see Supporting Information, Section S4). We denote the distance between these two maxima as Δ. Both L_{MMI} and Δ are the key parameters in the design of MMI couplers and are governed by the width W of the multimode waveguide. Parts a–c of Figure 3 demonstrate LRM images measured for multimode waveguides of different width: W = 2.1, 3.5, 4.5 μm. The first single self-image position continuously shifts from the beginning of MMI waveguide to its end with the W increase. The distance Δ increases with the W growth as well. To analyze $L_{MMI}(W)$ dependence, we measured the intensity profile along the MMI waveguide center for various W values. The studied longitudinal section is marked with a horizontal red line in the LRM images. The intensity distribution along the line is a series of peaks and dips associated with odd self-images (single, 3-fold, *etc.*) and even self-images (2-fold, 4-fold, *etc.*), respectively. Figure 3d shows the experimental results for W values from 1.7 to 4.5 μm with the step of 0.2 μm. Each horizontal line in the 3D graph corresponds to the longitudinal intensity distribution along the waveguide with a particular W value. The corresponding BSW near-field intensity profiles calculated as a function of W are presented in Figure 3e for

https://dx.doi.org/10.1021/acsnano.0c04301
ACS Nano 2020, 14, 10428–10437

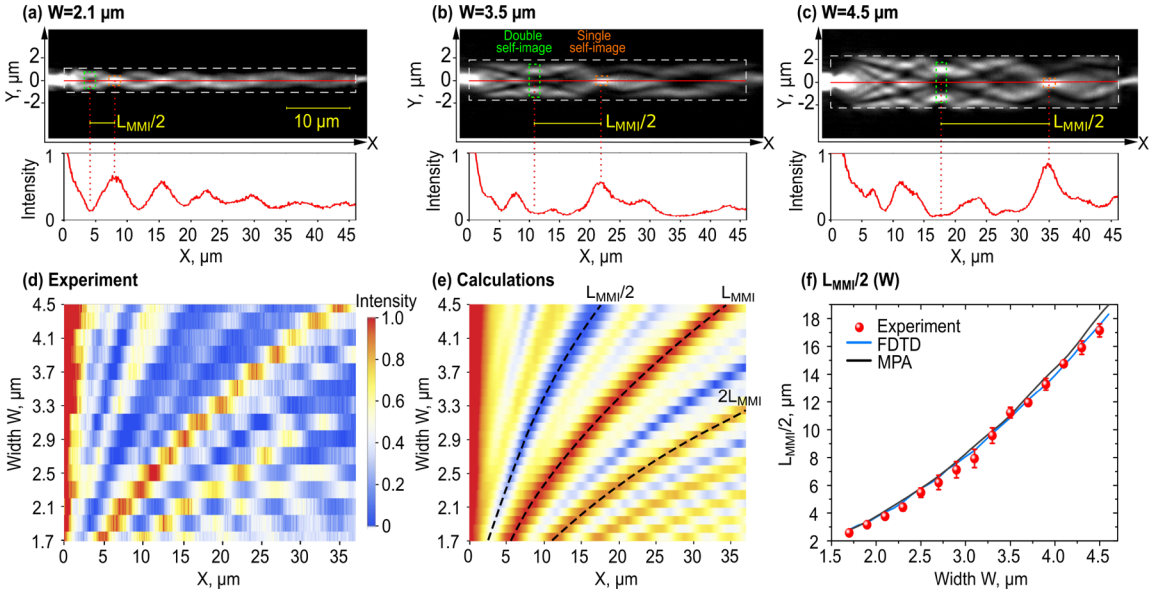

Figure 3. Multimode interference period of Bloch surface waves. (a–c) (Top) LRM images of the waveguides with the width W = 2.1, 3.5, 4.5 μm, respectively. (Bottom) Leakage radiation intensity distribution along the waveguide center marked by the red line in the LRM image. (d, e) Experimental and numerical dependences of the leakage radiation intensity and near-field intensity distributions along the waveguide on its width. Dashed curves indicate positions of the dips and peaks corresponding to the first 2-fold, first single, and second singe self-images. (f) Dependence of the MMI half period $L_{MMI}/2$ on the waveguide width W. Experimental data is shown with red dots, numerical data obtained from FDTD simulation is shown with a blue curve, numerical data obtained from MPA using eq 1 is shown with a black curve.

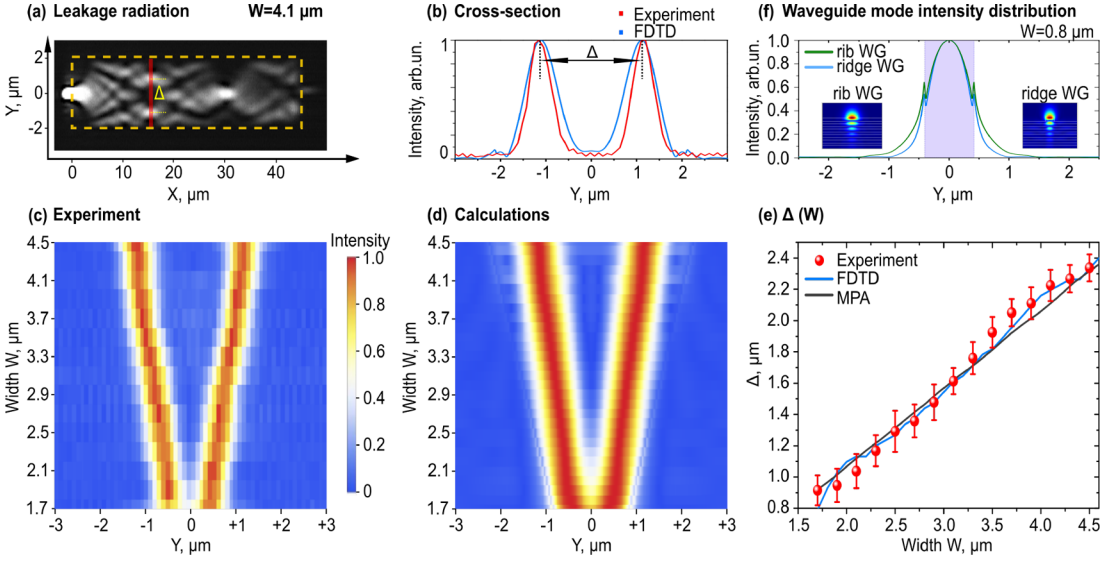

Figure 4. Two-fold self-image characterization. (a) LRM image of the waveguide with W = 4.1 μm. Red line is the position of the first 2-fold self-image. (b) Leakage radiation intensity (red curve) and near-field amplitude (blue curve) distributions in the position of the 2-fold self-image. (c, d) Experimental and numerical dependences of leakage radiation intensity and near-field amplitude distributions of the 2-fold self-image on the waveguide width. (e) Dependence of the distance Δ between BSW intensity maxima in the 2-fold self-image on the waveguide width W. Experimental data is shown with red dots, numerical data obtained from FDTD simulation is shown with a blue curve, and numerical data obtained from MPA using eq 1 and 2 is shown with a black line. (f) Calculated BSW intensity profiles in cross-section of the single-mode waveguides with various cladding effective refractive indices. Insets show the intensity distribution of TE_{00} BSW mode in the rib and ridge waveguide configurations.

comparison. With increasing width, a change in the position of the maximum corresponding to the first single self-image is easily observed. Dashed curves in Figure 3e schematically show the evolution of the positions of the first 2-fold, first single, and second single self-images, demonstrating a nonlinear growth of L_{MMI} distance with the waveguide width increase. Due to inevitable radiation losses, the MMI patterns become blurry moving along the waveguide. The losses associated with the light scattering on inhomogeneities of the waveguide were not taken into account in the calculations that leads to a slight mismatch between LRM intensity and near-field intensity distributions.

Experimental MMI patterns allow us to extract the values of longitudinal distance $L_{MMI}/2$ between the positions of all single and 2-fold self-images and average them for each W (see Supporting Information, Section S5). The obtained depend-

https://dx.doi.org/10.1021/acsnano.0c04301
ACS Nano 2020, 14, 10428–10437

ence of $L_{MMI}/2$ on W is shown in Figure 3f by red dots. The dependence demonstrates a nearly quadratic growth of the BSW MMI period with the waveguide width increase. $L_{MMI}/2$ values taken from FDTD near-field calculations and averaged in the same manner are marked by the blue curve in Figure 3f. The measurements agree well with the calculations indicating that the LRM measurements not only qualitatively but also quantitatively reproduce the calculated near-field distribution of BSW modes in the MMI structures. Note that the BSW scattering losses do not affect the value of the MMI period.

In the same way, we analyze the dependence of distance Δ between the BSW intensity maxima in the 2-fold image on the width of the MMI waveguide. The results are shown in Figure 4. For each W, we measured the intensity profile across the multimode waveguide at the position of the first 2-fold self-image. As an example, the LRM image of the 4.1 μm wide multimode waveguide with the cross-section position marked by the vertical red line and corresponding intensity profile normalized to its maximum intensity are shown in parts a and b, respectively, of Figure 4. Combined experimental results for all W values are presented in Figure 4c, where each horizontal line is normalized intensity profile corresponding to particular W value. The results of FDTD near-field calculations are given in Figure 4d for comparison. Experimental and calculated dependences $\Delta(W)$ obtained from the intensity profiles are shown by red dots and a blue curve in Figure 4e, correspondingly. The distance between the maxima in the 2-fold self-image almost linearly depends on the width of the multimode waveguide.

Multimode interference effects are well described by the guided-mode propagation analysis developed for step-index waveguides,[41] according to which L_{MMI} is proportional to the beat length L_π of the two lowest order modes

$$L_\pi = \frac{\pi}{(\beta_0 - \beta_1)} \simeq \frac{4 n_r W_e^2}{3\lambda_0} \quad (1)$$

where β_0 and β_1 are propagation constants of these modes (TE_{00} and TE_{01} in our case), n_r is an effective refractive index of the waveguide core (which corresponds to the effective refractive index n_{eff}^{max} of the BSW in polymer film on top of the PC in our case, see Supporting Information, Section S2), W_e is an effective fundamental mode width, which is proportional to the waveguide width W, and λ_0 is the wavelength of incident radiation in vacuum. In our case, the input waveguide enters the center of the multimode waveguide resulting in the excitation of even symmetric modes only. This symmetric interference has the minimum value of the MMI period of $L_{MMI} = 3L_\pi/4$. It is easy to find the $L_{MMI}(W)$ dependence calculating the difference $n_{eff}^{TE_{00}} - n_{eff}^{TE_{01}}$ between effective refractive indices of two lowest order modes using any eigenmode solver (we used Lumerical FDE solver). The result for $L_{MMI}/2(W)$ is presented in Figure 3f by the black line. The perfect agreement of numerical results with the ones obtained from the experiment and the FDTD calculations indicates that BSW propagating in MMI waveguides is successfully described by the mode propagation analysis (MPA) originally developed for conventional step-index waveguides.

According to MPA approach, the distance Δ should be exactly equal to the half of the width W_e of fundamental waveguide mode[41]

$$\Delta = \frac{W_e}{2} = \frac{W}{2} + \frac{\delta W}{2} \quad (2)$$

$$\delta W = \frac{\lambda_0}{\pi\sqrt{n_r^2 - n_c^2}} \quad (3)$$

where δW is the penetration depth of the BSW mode field into the cladding material and n_c is effective refractive index of the cladding. We calculated W_e for each W using the eq 1 and obtained $\Delta(W)$ dependence, which is shown in Figure 4e by a black curve and is in good agreement with the measurements and FDTD calculations. Using eq 2, we found $\delta W/2 = 65$ nm from this dependence. The best linear fit of the experimental $\Delta(W)$ dependence by the eq 2 provides $\delta W/2 = 89 \pm 18$ nm which is quite close to the calculated value. Further, the mean value of refractive index contrast $n_r^2 - n_c^2 = 2.7$ is calculated using eq 3 with the experimental value of $\delta W/2 = 89$ nm. Given that $n_r = n_{eff}^{max} = 1.13$, we conclude that the cladding effective refractive index n_c is a complex number with a large imaginary part. This is because the medium outside the waveguide acts like PC in the band gap region, since bare PC does not support BSWs outside the waveguide. In the situation when PC sustains BSW inside and outside of waveguide,[14,33,35] n_c is equal to BSW n_{eff} on a bare PC as was demonstrated in BSW refraction experiments.[50] In addition, n_r can be controlled more or less independently of n_c by the choice of the waveguide height. Such flexibility can be shown by the example of our PC. Lets consider two types of single-mode waveguides with the same width of 0.8 μm. The first type is the ridge waveguide studied in this paper. The second one is a rib waveguide of 60 nm height located on a 150 nm thick polymer layer that covers the PC. Waveguide effective refractive index n_r is the same in both cases, but the values of n_c are different since in the second case the PC/polymer layer structure sustains BSW with $n_{eff} = 1.01$ outside the rib waveguide. Figure 4f demonstrates intensity distribution of BSW fundamental mode in the waveguides cross-section at the height of 160 nm from Ta_2O_5 layer. The lateral field confinement is better in the ridge waveguide since the index contrast $n_r^2 - n_c^2$ is higher in this case. Thus, the BSW integrated platform provides an opportunity to choose the desired refractive index contrast from hundredths and tenths to several units, *i.e.*, implement low or high contrast system based on ones purposes. This can be useful, for example, in managing the evanescent coupling of waveguides placed in close proximity since the greater is the contrast the weaker the interaction between the waveguides is. Furthermore, the ability to create a high refractive index contrast on the BSW platform significantly reduces the curvature radius of BSW waveguides, as shown in Supporting Information, Section S4.

Mach–Zehnder Interferometer. We demonstrated the possibility of controlling BSW using the MMI effect by creating compact Mach–Zehnder interferometers (MZIs) with a desirable phase shift between BSW modes propagating in two arms without curved parts. MZI consisting of 1 × 2 and 2 × 1 MMI couplers connected by two arms with different optical paths for fundamental BSW mode is shown in Figure 5a. The necessary phase shift is provided by a 1 × 1 MMI coupler in one of the arms.

Effective refractive index of a waveguide mode rises with the increase of the waveguide width. Thus, the phase shift in the arm of the interferometer can be induced by the waveguide

https://dx.doi.org/10.1021/acsnano.0c04301
ACS Nano 2020, 14, 10428–10437

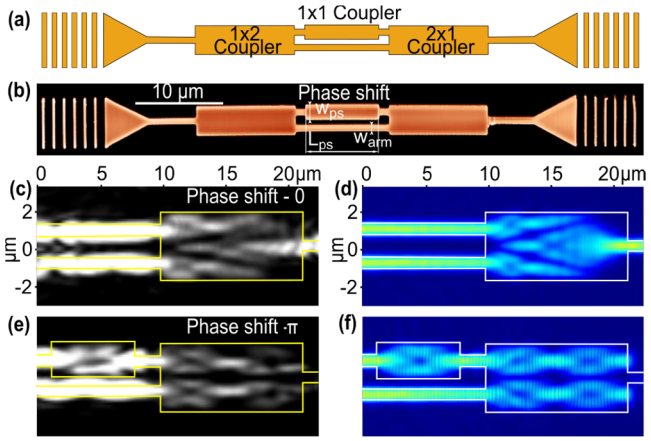

Figure 5. Mach−Zehnder interferometers for Bloch surface waves. (a) Scheme of MZI with a non-zero phase shift between the BSW modes propagating in different arms. (b) AFM image of MZI with the phase shift of π. (c, e) Experimental LRM images of the right part of MZIs with the phase shift of 0 and π, respectively. (d, f) Calculated near-field distribution in the right part of MZIs with the phase shift of 0 and π.

with different width put in the arm. The value of the phase shift is defined as follows

$$\Delta\varphi = \frac{2\pi}{\lambda_0}(n_{\mathrm{eff}}^{\mathrm{TE}_{00}}(W_{\mathrm{ps}}) - n_{\mathrm{eff}}^{\mathrm{TE}_{00}}(W_{\mathrm{arm}}))L_{\mathrm{ps}} \quad (4)$$

where $n_{\mathrm{eff}}^{\mathrm{TE}_{00}}(W_{\mathrm{arm}})$ and $n_{\mathrm{eff}}^{\mathrm{TE}_{00}}(W_{\mathrm{ps}})$ are effective refractive indices of fundamental TE_{00} mode in narrow and wide parts of waveguides with the width of W_{arm} and W_{ps}, respectively, L_{ps} is the length of the wide waveguide part, and λ_0 is the wavelength of the light in vacuum. The specific phase shift $\Delta\varphi$ can be achieved by infinite set of configurations of (W_{ps}; L_{ps}). However, shorter values of L_{ps} are preferred for compact MZI device. This can be achieved by increasing the difference of n_{eff} in eq 4, which grows with the increase of $W_{\mathrm{ps}} - W_{\mathrm{arm}}$ widths' mismatch. On the contrary, the increase of W_{ps} leads to the MMI effect. The critical width W_{ps} of the wide waveguide for studied BSW structures is equal to 1.6 μm when TE_{02} mode can be excited. With the further increase of W_{ps}, we have to fix the length L_{ps} equal to L_{MMI} (W_{ps}) in order to avoid losses. As a result, the wide part of the waveguide becomes 1 × 1 MMI coupler, and the specific phase shift is achievable only for a single configuration of (W_{ps}; L_{ps}) (see Supporting Information, Section S6).

We designed two MZIs with the phase shift of 0 and π. In the 0-phase-shift case, two MZI arms are identical single-mode waveguides with the constant width W_{arm} = 0.8 μm and the length of 10 μm. The π-phase-shift MZI contains a section of the wide multimode waveguide with the width W_{ps} = 1.9 μm and the length L_{ps} = 7 μm, which is embedded in the single-mode waveguide of one of the arms, as shown in the AFM image in Figure 5b. The distance between the phase shift waveguide and the second arm waveguide is fixed to 0.5 μm to eliminate a potential crosstalk between them. This results in the distance of 1.9 μm between output waveguides of the 1 × 2 coupler. Using experimental dependences of $L_{\mathrm{MMI}}(W)$ and $\Delta(W)$ from Figure 3f and Figure 4e we have found the width and length of 1 × 2 MZI couplers, which are 3.6 and 11.4 μm, respectively. Experimental LRM images as well as numerically calculated near-field intensity distributions in two MZIs are shown in Figure 5 c,e and Figure 5 d,f, respectively. Constructive and destructive interference in the output waveguide is clearly seen for MZIs with phase shifts of 0 and π, correspondingly (see Supporting Information, Section S7, about losses in MMI couplers and MZIs). The experimental LRM field distributions are in a good agreement with the near-field distribution calculated by FDTD. This result demonstrates the ability to well control and manipulate visible light at the microscale using BSW concept.

CONCLUSIONS

We have experimentally demonstrated the effect of multimode interference of Bloch surface waves by a direct visualization of the interference pattern using leakage radiation microscopy technique. We measured the dependences of the MMI period and the distance between two images in the first 2-fold self-image on the width of the multimode waveguide. Excellent qualitative and quantitative agreement of the experimentally measured leakage radiation intensity distributions in a multimode waveguide with the near-field distributions obtained from 3D FDTD simulations is demonstrated. This confirms wide possibilities of the LRM method to determine the near-field characteristics of leaky modes. We have also shown that MMI of BSWs with a complex field distribution inside the PC is perfectly described by the mode propagation analysis that was originally developed for the bulk guided modes propagating in step-index waveguides. This allows us to estimate the size of the MMI couplers without resorting to time-consuming three-dimensional simulations, but using the effective refractive indices of the first two modes, which can be obtained with the eigenmode solvers. Finally, based on the results of studying the MMI effect, we demonstrated Mach−Zehnder interferometers with a predefined phase difference between the BSWs propagating in different arms. Interferometers operate in the visible wavelength range and do not contain the curved parts.

We used the PC comprising only five pairs of layers in order to obtain the BSWs with sufficient radiation losses and make it easy to detect through the leakage radiation. However, the radiation losses decrease exponentially with increasing the number of PC periods and can be made negligible. For example, the recent study experimentally demonstrates the BSW with the losses of only 3 dB/cm at the wavelength of 633 nm,[15] which is one or 2 orders of magnitude smaller than the losses reported for all types of surface electromagnetic waves in the visible and comparable with losses of Si_3N_4 waveguides.[51] This makes the BSW platform very promising for its application in visible integrated photonics, development of which is essential in areas such as quantum optics, harmonic generation, on-chip light sources, and biosensing. Notably, the proposed photonic devices sustain the guided modes with a quite low effective refractive index close to unity. Despite this, BSW MMI elements are comparable in size to typical MMI structures for dielectric-loaded SPP[52] and high-refractive-index SOI platform.[53] According to eq 1, the MMI period determining the size of MMI device is proportional to the ratio n_r/λ for a fixed width W_e approximately equal to W for the SOI and proposed BSW cases. For our waveguides n_r/λ = 1.13/0.67 = 1.69 μm^{-1}, while for SOI waveguides n_r is about 2.8−2.9[54] and n_r/λ = 2.85/1.55 = 1.84 μm^{-1}. Surprisingly, the length of the BSW device designed for 1.55 μm wavelength should be almost 2.5 times shorter than that of the SOI device with the same width, which actually results from fewer interfering modes supported by the BSW multimode wave-

https://dx.doi.org/10.1021/acsnano.0c04301
ACS Nano 2020, 14, 10428−10437

guide. However, the minimum width of MMI devices is limited by the cutoff waveguide width of the second mode (TE_{01} or TM_{01}), which is 1.7λ in our case and, in theory, reaches 0.4λ for SOI and dielectric-loaded SPP[7] platforms. In turn, the ability to use the smallest possible number of modes, when designing couplers with a large number of inputs and outputs, is an important advantage of BSW MMI devices, because it allows us to minimize the influence of the phase errors occurring for high-order modes[55] and improve the performance of large couplers without tricks such as creating subdiffraction structuring.[56] The possibility of using the BSW platform to easily design the effective refractive index contrast by simply adjusting the thicknesses of PC layers and top structured layer enables us to further reduce the phase errors for higher-orders waveguide modes.[57]

In summary, our work is a clear demonstration of how well visible light can be manipulated on a micrometer scale using conventional dielectric materials and simple structuring techniques. The BSW platform provides opportunities to design the integrated photonic circuits for specific spectral ranges in which SPP or SOI platforms suffer from absorption. The BSW devices under the development can be easily inspected at the prototyping stage by the LRM technique that allows visualizing the influence of defects and fabrication errors on the near-field distribution inside the devices. The confinement of the BSW field near the top of a waveguide (unlike dielectric-loaded surface plasmon-polaritons[7]) ensures its sensitivity to the environment, which reveals the way of implementing BSW-based integrated optical sensors for applications in biology and medicine. Moreover, the ability to use polymers as a waveguide core material allows us to incorporate various types of luminescence or nonlinear materials, such as quantum dots, directly into the waveguides making BSW devices active. Alternatively, active devices can be fabricated on the surface of a photonic crystal with nonlinear layers.[58] We believe that the proposed MMI concept can form the foundation of integrated optical devices that are applicable to a number of key tasks, such as integrated single-photon sources[59] and on-chip quantum circuits,[2] and integrated photonic sensors[60] including multimode interference devices for sensing.

METHODS

Photonic Crystal Samples. One-dimensional photonic crystal (PC) is designed to sustain TE-polarized BSW at λ = 670 nm in the presence of an additional layer of polymer on its surface (see Supporting Information, Section S1 for details). It consists of five pairs of SiO_2 (n_{SiO_2} = 1.45 at λ = 670 nm) and Ta_2O_5 ($n_{Ta_2O_5}$ = 2.09 at λ = 670 nm) alternating layers sputtered on a BK-7 glass coverslip (n_{sb} = 1.52) with a thickness of 170 μm. The thicknesses of the SiO_2 and Ta_2O_5 layers are 140 and 98 nm, respectively. The terminating layer of PC is Ta_2O_5. The thickness of the polymer film on the PC surface is an important parameter and defines the height of the waveguides. In order to make a thin film the photoresist SU-8 2015 (Microchem, n_{SU-8} = 1.58) is first diluted with SU-8 developer of mr-DEV 600 (Microchem) in a ratio of 15:85, and the obtained solution is spin coated at 3000 rpm to obtain 210 nm thick polymer layer.

MMI Sample Fabrication. The fabrication procedure of MMI samples consists of five steps: photoresist film spin-coating, prebaking at 95 °C for 45 min (solvent evaporation), exposure (writing), baking at 95 °C for 15 min (SU-8 polymerization), developing in mr-dev600. Exposure is performed with the custom two-photon laser lithography setup.[36] Radiation from the femtosecond Ti:sapphire laser source (Coherent Vitara, λ = 800 nm, 50 fs pulse duration, 80 MHz repetition rate) is focused on the PC surface with an air objective lens (NA = 0.95, 100X, LOMO) mounted on a piezo stage (Newport NPO250SG). Fast steering mirror (Newport FSM300) combined with a 4*f*-system provides rapid lateral beam movement. An acousto-optic modulator (Isomet M1099-T80L-3) is used as a fast beam shutter. The writing trajectories are straight lines. Grating hatches and single-mode waveguides are single lines, tapers consist of an array of lines with smoothly changing length. Multimode waveguide is an array of parallel lines with the same length. The distance between subsequent lines in arrays is 200 nm. The width of multimode waveguides is controlled by the number of parallel lines with an accuracy of less than 30 nm. The writing speed is 10 μm/s, and the average power at the entrance of the objective lens is 15 mW. Writing is performed in an overexposure regime resulting in a waveguide profile close to the rectangular shape as can be seen in Figure 2b.

MMI Samples. MMI structures consist of a diffraction grating, taper, narrow input single-mode waveguide, wide multimode waveguide, and narrow output waveguide. The diffraction grating contains six hatches with a period of 1340 nm. The taper is an isosceles triangle with a base of 5 μm and a length of 6 μm. The input 0.8 μm waveguide is located in the middle of the wide multimode waveguide. This design implements so-called symmetric mechanism of interference,[41] providing the shortest MMI period. The length of both input and output waveguides is equal to 15 μm. The length of the multimode waveguide is 46 μm, while the width W is varied from 1.7 to 4.5 μm with a 0.2 μm step. For each W, we fabricated 5 MMI structures with the same parameters to then average the results for the $L_{MMI}/2$ and Δ over identical samples. The geometrical parameters of MZI diffraction gratings, tapers, and single-mode waveguides are equal to those described above.

Leakage Radiation Microscopy. MMI structures and MZIs are characterized using leakage radiation microscopy. LRM allows visualization of BSW propagation as well as wavevector distribution of BSW modes. A collimated beam of 670 nm laser diode (Thorlabs CPS670F) is focused by an objective lens (NA = 0.2, 10X, Lomo) mounted on a three-axis stage into the input grating of MMI structure at the normal angle of incidence. The polarization of the incident radiation is controlled by Glan-Taylor prism. The imaging part of LRM setup is based on an oil immersion objective lens with a high numerical aperture (NA= 1.3, 100×, Olympus UPLFLN100XOI2) allowing us to collect TE-polarized leakage radiation of BSW waveguide modes with $n_{eff} \leq 1.3$. The collected light passes through the 4*f*-system in order to perform two-stage filtering in real and **k**-space. This system constructs intermediate images of front and back focal planes of the collecting objective lens. Filtering is done with an aperture and slit located in the intermediate images of front and back focal planes of the objective lens, respectively. At the first filtering stage, the aperture selects a part of collected radiation that comes only from the MMI region of waveguide structures (dotted line in the Figure 1). At the second stage, the slit selects the radiation with the value of the tangential component of wavevector from k_0 to 1.2 k_0. The back focal plane image of leakage radiation of BSW waveguide mode is a strip perpendicular to the direction of BSW propagation.[27,48] Thus, the edges of the slit are oriented in parallel to the stripes to pass all the leakage radiation. After filtering, the front and back focal plane images are constructed on the sensors of two different CMOS cameras (Thorlabs DCC1545M) allowing us to study BSW field and wavevector distribution simultaneously. The polarization of collected radiation is controlled by a film polarizer. The additional information on LRM setup is provided in Supporting Information, Section S3.

Calculations. Numerical calculations are performed with the commercial Lumerical FDTD software. The simulation area is set to be 3D. SiO_2 and Ta_2O_5 PC layers are modeled as dielectrics with refractive indices equal to 1.45 and 2.09 and thicknesses of 140 and 98 nm, respectively. The PC is on a glass substrate with refractive index equal to 1.52 and thickness equal to 2 μm. Polymer waveguides (single-mode and multimode) are modeled as a ridge with refractive index equal to 1.58. The height of the waveguides is fixed to 210 nm during calculations. First, we study BSW modes of a polymer waveguide with the Lumerical FDE solver. A two-dimensional slice of

https://dx.doi.org/10.1021/acsnano.0c04301
ACS Nano 2020, 14, 10428−10437

the PC with the waveguide at the top is used to evaluate BSW modes sustained by the waveguide. Thus, we obtain effective refractive indices for all modes supported by a waveguide with a particular width. Then we evaluate the dependence of TE_{00} and TE_{01} BSW mode effective refractive indices on the waveguide width. These data are used to calculate MMI half period $L_{MMI}/2$ and effective waveguide width W_e using eqs 1−3 (see Supporting Information, Section 2). Then the TE_{00} BSW mode is launched into the input single-mode waveguide of the studied MMI structure to perform 3D FDTD simulation. The model of the MMI structure on top of the PC consists of the input single-mode waveguide with a length of 5 μm and a width of 0.8 μm and the wide multimode waveguide with a length of 46 μm and a width from 1.7 to 4.5 μm. The near-field distribution is measured in the plane parallel to the PC surface and located at the distance of 160 nm above the PC surface. This position corresponds to the maximum of the BSW electromagnetic field intensity. The simulation volume is enclosed in the Perfectly Matched Layers (PML) boundary condition.

ASSOCIATED CONTENT

Supporting Information

The Supporting Information is available free of charge at https://pubs.acs.org/doi/10.1021/acsnano.0c04301.

Numerical design of the photonic crystal; effective refractive indicies of BSW waveguide modes and the proof of the applicability of the mode propagation analysis to the BSW mode description; scheme and detailed description of the leakage radiation microscopy setup; demonstration of 1 × 2 multimode interference BSW splitter, estimation of losses in BSW waveguides; description of camera images processing for determination of multimode interference parameters; design of a multimode interference BSW phase shifter; estimation of losses in BSW MMI structures (PDF)

AUTHOR INFORMATION

Corresponding Author

Vladimir O. Bessonov − *Faculty of Physics, Lomonosov Moscow State University, Moscow 119991, Russia; Frumkin Institute of Physical Chemistry and Electrochemistry, Russian Academy of Sciences, Moscow 119071, Russia;* orcid.org/0000-0002-2165-1924; Phone: +7 (495) 939-39-10; Email: bessonov@nanolab.phys.msu.ru

Authors

Kirill R. Safronov − *Faculty of Physics, Lomonosov Moscow State University, Moscow 119991, Russia*

Dmitry N. Gulkin − *Faculty of Physics, Lomonosov Moscow State University, Moscow 119991, Russia*

Ilya M. Antropov − *Faculty of Physics, Lomonosov Moscow State University, Moscow 119991, Russia*

Ksenia A. Abrashitova − *Faculty of Physics, Lomonosov Moscow State University, Moscow 119991, Russia*

Andrey A. Fedyanin − *Faculty of Physics, Lomonosov Moscow State University, Moscow 119991, Russia;* orcid.org/0000-0003-4708-6895

Complete contact information is available at: https://pubs.acs.org/10.1021/acsnano.0c04301

Author Contributions

K.R.S. initiated research and performed calculations. K.R.S., V.O.B., and A.A.F. conceived and planned the experiments. V.O.B. designed leakage radiation microscopy setup. D.N.G. conducted leakage radiation microscopy experiments. I.M.A. prepared thin polymer films and performed atomic force microscopy measurements. K.A.A. and K.R.S. fabricated BSW waveguide samples. K.R.S., V.O.B., and A.A.F. wrote the manuscript, D.N.G. compiled the figures. All authors contributed to the discussion of the results and the manuscript. V.O.B. and A.A.F. supervised the entire project.

Notes

The authors declare no competing financial interest.

ACKNOWLEDGMENTS

This work was partly supported by Russian Ministry of Education and Science (14.W03.31.0008, photonic crystal fabrication and leakage radiation microscopy setup), Russian Foundation for Basic Research (18-32-00869, 18-32-00841), and MSU Quantum technology centre.

REFERENCES

(1) Cheben, P.; Halir, R.; Schmid, J. H.; Atwater, H. A.; Smith, D. R. Subwavelength Integrated Photonics. *Nature* **2018**, *560*, 565−572.

(2) Wang, J.; Paesani, S.; Ding, Y.; Santagati, R.; Skrzypczyk, P.; Salavrakos, A.; Tura, J.; Augusiak, R.; Mančinska, L.; Bacco, D.; Bonneau, D.; Silverstone, J. W.; Gong, Q.; Acín, A.; Rottwitt, K.; Oxenløwe, J. L.; Leif, K.; O'Brien; Laing, A.; Thompson, M. G. Multidimensional Quantum Entanglement with Large-Scale Integrated Optics. *Science* **2018**, *360*, 285−291.

(3) Wörhoff, K.; Heideman, R. G.; Leinse, A.; Hoekman, M. TriPleX: A Versatile Dielectric Photonic Platform. *Adv. Opt. Technol.* **2015**, *4*, 189−207.

(4) Ebbesen, T. W.; Genet, C.; Bozhevolnyi, S. I. Surface-Plasmon Circuitry. *Phys. Today* **2008**, *61*, 44−50.

(5) Azzini, S.; Lheureux, G.; Symonds, C.; Benoit, J.-M.; Senellart, P.; Lemaitre, A.; Greffet, J.-J.; Blanchard, C.; Sauvan, C.; Bellessa, J. Generation and Spatial Control of Hybrid Tamm Plasmon/Surface Plasmon Modes. *ACS Photonics* **2016**, *3*, 1776−1781.

(6) Takayama, O.; Artigas, D.; Torner, L. Lossless Directional Guiding of Light in Dielectric Nanosheets Using Dyakonov Surface Waves. *Nat. Nanotechnol.* **2014**, *9*, 419−424.

(7) Holmgaard, T.; Bozhevolnyi, S. I. Theoretical Analysis of Dielectric-Loaded Surface Plasmon-Polariton Waveguides. *Phys. Rev. B: Condens. Matter Mater. Phys.* **2007**, *75*, 245405.

(8) Yeh, P.; Yariv, A.; Cho, A. Optical Surface Waves in Periodic Layered Media. *Appl. Phys. Lett.* **1978**, *32*, 104−105.

(9) Meade, R. D.; Brommer, K. D.; Rappe, A. M.; Joannopoulos, J. Electromagnetic Bloch Waves at the Surface of a Photonic Crystal. *Phys. Rev. B: Condens. Matter Mater. Phys.* **1991**, *44*, 10961.

(10) Khan, M. U.; Corbett, B. Bloch Surface Wave Structures for High Sensitivity Detection and Compact Waveguiding. *Sci. Technol. Adv. Mater.* **2016**, *17*, 398−409.

(11) Badugu, R.; Mao, J.; Blair, S.; Zhang, D.; Descrovi, E.; Angelini, A.; Huo, Y.; Lakowicz, J. R. Bloch Surface Wave-Coupled Emission at Ultraviolet Wavelengths. *J. Phys. Chem. C* **2016**, *120*, 28727−28734.

(12) Descrovi, E.; Sfez, T.; Dominici, L.; Nakagawa, W.; Michelotti, F.; Giorgis, F.; Herzig, H. P. Near-Field Imaging of Bloch Surface Waves on Silicon Nitride One-Dimensional Photonic Crystals. *Opt. Express* **2008**, *16*, 5453−5464.

(13) Smolik, G. M.; Descharmes, N.; Herzig, H. P. Toward Bloch Surface Wave-Assisted Spectroscopy in the Mid-Infrared Region. *ACS Photonics* **2018**, *5*, 1164−1170.

(14) Dubey, R.; Barakat, E.; Häyrinen, M.; Roussey, M.; Honkanen, S.; Kuittinen, M.; Herzig, H. P. Experimental Investigation of the Propagation Properties of Bloch Surface Waves on Dielectric Multilayer Platform. *J. Eur. Opt. Soc.-Rapid* **2017**, *13*, 5.

(15) Lahijani, B. V.; Descharmes, N.; Barbey, R.; Osowiecki, G. D.; Wittwer, V. J.; Razskazovskaya, O.; Südmeyer, T.; Herzig, H. P. Optical Surface Waves on One-Dimensional Photonic Crystals: Investigation of Loss Mechanisms and Demonstration of Centi-

https://dx.doi.org/10.1021/acsnano.0c04301
ACS Nano 2020, 14, 10428−10437

meter-Scale Propagation. *arXiv:physics/1907.00187*, 2019, https://arxiv.org/abs/1907.00187 (accessed 2019-06-29).
(16) Sinibaldi, A.; Danz, N.; Descrovi, E.; Munzert, P.; Schulz, U.; Sonntag, F.; Dominici, L.; Michelotti, F. Direct Comparison of the Performance of Bloch Surface Wave and Surface Plasmon Polariton Sensors. *Sens. Actuators, B* **2012**, *174*, 292−298.
(17) Kuai, Y.; Chen, J.; Tang, X.; Xiang, Y.; Lu, F.; Kuang, C.; Xu, L.; Shen, W.; Cheng, J.; Gui, H.; Zou, G.; Wang, P.; Ming, H.; Liu, J.; Liu, X.; Lakowicz, J. R.; Zhang, D. Label-Free Surface-Sensitive Photonic Microscopy with High Spatial Resolution Using Azimuthal Rotation Illumination. *Sci. Adv.* **2019**, *5*, No. eaav5335.
(18) Shilkin, D. A.; Lyubin, E. V.; Soboleva, I. V.; Fedyanin, A. A. Direct Measurements of Forces Induced by Bloch Surface Waves in a One-Dimensional Photonic Crystal. *Opt. Lett.* **2015**, *40*, 4883−4886.
(19) Pirotta, S.; Xu, X.; Delfan, A.; Mysore, S.; Maiti, S.; Dacarro, G.; Patrini, M.; Galli, M.; Guizzetti, G.; Bajoni, D.; Sipe, J. E.; Walker, G. C.; Liscidini, M. Surface-Enhanced Raman Scattering in Purely Dielectric Structures *via* Bloch Surface Waves. *J. Phys. Chem. C* **2013**, *117*, 6821−6825.
(20) Barachati, F.; Fieramosca, A.; Hafezian, S.; Gu, J.; Chakraborty, B.; Ballarini, D.; Martinu, L.; Menon, V.; Sanvitto, D.; Kéna-Cohen, S. Interacting Polariton Fluids in a Monolayer of Tungsten Disulfide. *Nat. Nanotechnol.* **2018**, *13*, 906−909.
(21) Lerario, G.; Ballarini, D.; Fieramosca, A.; Cannavale, A.; Genco, A.; Mangione, F.; Gambino, S.; Dominici, L.; De Giorgi, M.; Gigli, G.; Sanvitto, D. High-Speed Flow of Interacting Organic Polaritons. *Light: Sci. Appl.* **2017**, *6*, No. e16212.
(22) Soboleva, I.; Moskalenko, V.; Fedyanin, A. Giant Goos-Hänchen Effect and Fano Resonance at Photonic Crystal Surfaces. *Phys. Rev. Lett.* **2012**, *108*, 123901.
(23) Romodina, M.; Soboleva, I.; Musorin, A.; Nakamura, Y.; Inoue, M.; Fedyanin, A. Bloch-Surface-Wave-Induced Fano Resonance in Magnetophotonic Crystals. *Phys. Rev. B: Condens. Matter Mater. Phys.* **2017**, *96*, No. 081401.
(24) Konopsky, V. N.; Alieva, E. V.; Alyatkin, S. Y.; Melnikov, A. A.; Chekalin, S. V.; Agranovich, V. M. Phase-Matched Third-Harmonic Generation *via* Doubly Resonant Optical Surface Modes in 1D Photonic Crystals. *Light Sci. Appl.* **2016**, *5*, No. e16168.
(25) Soboleva, I.; Descrovi, E.; Summonte, C.; Fedyanin, A.; Giorgis, F. Fluorescence Emission Enhanced by Surface Electromagnetic Waves on One-Dimensional Photonic Crystals. *Appl. Phys. Lett.* **2009**, *94*, 231122.
(26) Lereu, A. L.; Zerrad, M.; Passian, A.; Amra, C. Surface Plasmons and Bloch Surface Waves: Towards Optimized Ultra-Sensitive Optical Sensors. *Appl. Phys. Lett.* **2017**, *111*, No. 011107.
(27) Descrovi, E.; Barakat, E.; Angelini, A.; Munzert, P.; De Leo, N.; Boarino, L.; Giorgis, F.; Herzig, H. P. Leakage Radiation Interference Microscopy. *Opt. Lett.* **2013**, *38*, 3374−3376.
(28) Descrovi, E.; Giorgis, F.; Dominici, L.; Michelotti, F. Experimental Observation of Optical Bandgaps for Surface Electromagnetic Waves in a Periodically Corrugated One-Dimensional Silicon Nitride Photonic Crystal. *Opt. Lett.* **2008**, *33*, 243−245.
(29) Wang, R.; Wang, Y.; Zhang, D.; Si, G.; Zhu, L.; Du, L.; Kou, S.; Badugu, R.; Rosenfeld, M.; Lin, J.; Wang, P.; Ming, H.; Yuan, X.; Lakowicz, J. R. Diffraction-Free Bloch Surface Waves. *ACS Nano* **2017**, *11*, 5383−5390.
(30) Kovalevich, T.; Boyer, P.; Suarez, M.; Salut, R.; Kim, M.; Herzig, H. P.; Bernal, M.; Grosjean, T. Polarization Controlled Directional Propagation of Bloch Surface Wave. *Opt. Express* **2017**, *25*, 5710−5715.
(31) Zhang, D.; Wang, R.; Xiang, Y.; Kuai, Y.; Kuang, C.; Badugu, R.; Xu, Y.; Wang, P.; Ming, H.; Liu, X.; Lakowicz, J. R. Silver Nanowires for Reconfigurable Bloch Surface Waves. *ACS Nano* **2017**, *11*, 10446−10451.
(32) Wang, R.; Chen, J.; Xiang, Y.; Kuai, Y.; Wang, P.; Ming, H.; Lakowicz, J. R.; Zhang, D. Two-Dimensional Photonic Devices Based on Bloch Surface Waves with One-Dimensional Grooves. *Phys. Rev. Appl.* **2018**, *10*, No. 024032.
(33) Yu, L.; Barakat, E.; Sfez, T.; Hvozdara, L.; Di Francesco, J.; Herzig, H. P. Manipulating Bloch Surface Waves in 2D: A Platform Concept-Based Flat Lens. *Light: Sci. Appl.* **2014**, *3*, No. e124.
(34) Augenstein, Y.; Vetter, A.; Lahijani, B. V.; Herzig, H. P.; Rockstuhl, C.; Kim, M.-S. Inverse Photonic Design of Functional Elements That Focus Bloch Surface Waves. *Light: Sci. Appl.* **2018**, *7*, 104.
(35) Descrovi, E.; Sfez, T.; Quaglio, M.; Brunazzo, D.; Dominici, L.; Michelotti, F.; Herzig, H. P.; Martin, O.; Giorgis, F. Guided Bloch Surface Waves on Ultrathin Polymeric Ridges. *Nano Lett.* **2010**, *10*, 2087−2091.
(36) Abrashitova, K. A.; Gulkin, D. N.; Safronov, K. R.; Kokareva, N. G.; Antropov, I. M.; Bessonov, V. O.; Fedyanin, A. A. Bloch Surface Wave Photonic Device Fabricated by Femtosecond Laser Polymerisation Technique. *Appl. Sci.* **2018**, *8*, 63.
(37) Dubey, R.; Lahijani, B. V.; Häyrinen, M.; Roussey, M.; Kuittinen, M.; Herzig, H. P. Ultra-Thin Bloch-Surface-Wave-Based Reflector at Telecommunication Wavelength. *Photonics Res.* **2017**, *5*, 494−499.
(38) Wu, X.; Barakat, E.; Yu, L.; Sun, L.; Wang, J.; Tan, Q.; Herzig, H. Phase-Sensitive Near Field Investigation of Bloch Surface Wave Propagation in Curved Waveguides. *J. Eur. Opt. Soc.-Rapid* **2014**, *9*, 14049.
(39) Dubey, R.; Lahijani, B. V.; Barakat, E.; Häyrinen, M.; Roussey, M.; Kuittinen, M.; Herzig, H. P. Near-Field Characterization of a Bloch-Surface-Wave-Based 2D Disk Resonator. *Opt. Lett.* **2016**, *41*, 4867−4870.
(40) Rodriguez, G.; Aurelio, D.; Liscidini, M.; Weiss, S. Bloch Surface Wave Ring Resonator Based on Porous Silicon. *Appl. Phys. Lett.* **2019**, *115*, No. 011101.
(41) Soldano, L.; Pennings, E. Optical Multi-Mode Interference Devices Based on Self-Imaging: Principles and Applications. *J. Lightwave Technol.* **1995**, *13*, 615−627.
(42) Silverstone, J. W.; Bonneau, D.; Ohira, K.; Suzuki, N.; Yoshida, H.; Iizuka, N.; Ezaki, M.; Natarajan, C. M.; Tanner, M. G.; Hadfield, R. H.; Zwiller, V.; Marshall, G. D.; Rarity, J. G.; O'Brien, J. L.; Thompson, M. G. On-Chip Quantum Interference Between Silicon Photon-Pair Sources. *Nat. Photonics* **2014**, *8*, 104−108.
(43) Nakayama, K.; Tonooka, Y.; Ota, M.; Ishii, Y.; Fukuda, M. Passive Plasmonic Demultiplexers Using Multimode Interference. *J. Lightwave Technol.* **2018**, *36*, 1979−1984.
(44) Wang, F.; Yang, J.; Chen, L.; Jiang, X.; Wang, M. Optical Switch Based on Multimode Interference Coupler. *IEEE Photonics Technol. Lett.* **2006**, *18*, 421−423.
(45) Besse, P.; Bachmann, M.; Melchior, H.; Soldano, L.; Smit, M. Optical Bandwidth and Fabrication Tolerances of Multimode Interference Couplers. *J. Lightwave Technol.* **1994**, *12*, 1004−1009.
(46) Han, L.; Liang, S.; Zhu, H.; Qiao, L.; Xu, J.; Wang, W. Two-Mode De/Multiplexer Based on Multimode Interference Couplers with a Tilted Joint as Phase Shifter. *Opt. Lett.* **2015**, *40*, 518−521.
(47) Drezet, A.; Hohenau, A.; Koller, D.; Stepanov, A.; Ditlbacher, H.; Steinberger, B.; Aussenegg, F.; Leitner, A.; Krenn, J. Leakage Radiation Microscopy of Surface Plasmon Polaritons. *Mater. Sci. Eng., B* **2008**, *149*, 220−229.
(48) Wang, R.; Xia, H.; Zhang, D.; Chen, J.; Zhu, L.; Wang, Y.; Yang, E.; Zang, T.; Wen, X.; Zou, G.; Wang, P.; Ming, H.; Badugu, R.; Lakowicz, J. R. Bloch Surface Waves Confined in One Dimension with a Single Polymeric Nanofibre. *Nat. Commun.* **2017**, *8*, 1−10.
(49) Stepanov, A. L.; Krenn, J. R.; Ditlbacher, H.; Hohenau, A.; Drezet, A.; Steinberger, B.; Leitner, A.; Aussenegg, F. R. Quantitative Analysis of Surface Plasmon Interaction with Silver Nanoparticles. *Opt. Lett.* **2005**, *30*, 1524−1526.
(50) Sfez, T.; Descrovi, E.; Yu, L.; Quaglio, M.; Dominici, L.; Nakagawa, W.; Michelotti, F.; Giorgis, F.; Herzig, H. P. Two-Dimensional Optics on Silicon Nitride Multilayer: Refraction of Bloch Surface Waves. *Appl. Phys. Lett.* **2010**, *96*, 151101.
(51) Romero-García, S.; Merget, F.; Zhong, F.; Finkelstein, H.; Witzens, J. Silicon Nitride CMOS-Compatible Platform for Integrated

https://dx.doi.org/10.1021/acsnano.0c04301
ACS Nano 2020, 14, 10428−10437

Photonics Applications at Visible Wavelengths. *Opt. Express* **2013**, *21*, 14036−14046.
(52) Yuan, G.; Wang, P.; Lu, Y.; Ming, H. Multimode Interference Splitter Based on Dielectric-Loaded Surface Plasmon Polariton Waveguides. *Opt. Express* **2009**, *17*, 12594−12600.
(53) Zhou, H.; Song, J.; Li, C.; Zhang, H.; Lo, P. G. A Library of Ultra-Compact Multimode Interference Optical Couplers on SOI. *IEEE Photonics Technol. Lett.* **2013**, *25*, 1149−1152.
(54) Samanta, S.; Banerji, P.; Ganguly, P. Effective Index-Based Matrix Method for Silicon Waveguides in SOI Platform. *Optik* **2015**, *126*, 5488−5495.
(55) Ulrich, R.; Kamiya, T. Resolution of Self-Images in Planar Optical Waveguides. *J. Opt. Soc. Am.* **1978**, *68*, 583−592.
(56) Halir, R.; Bock, P. J.; Cheben, P.; Ortega-Moñux, A.; Alonso-Ramos, C.; Schmid, J. H.; Lapointe, J.; Xu, D.-X.; Wangüemert-Pérez, J. G.; Molina-Fernández, Í.; Janz, S. Waveguide Sub-Wavelength Structures: A Review of Principles and Applications. *Laser Photonics Rev.* **2015**, *9*, 25−49.
(57) Huang, J.; Scarmozzino, R.; Osgood, R. A New Design Approach to Large Input/Output Number Multimode Interference Couplers and Its Application to Low-Crosstalk WDM Routers. *IEEE Photonics Technol. Lett.* **1998**, *10*, 1292−1294.
(58) Kovalevich, T.; Belharet, D.; Robert, L.; Ulliac, G.; Kim, M.-S.; Herzig, H. P.; Grosjean, T.; Bernal, M.-P. Bloch Surface Waves at the Telecommunication Wavelength with Lithium Niobate as the Top Layer for Integrated Optics. *Appl. Opt.* **2019**, *58*, 1757−1762.
(59) Siampour, H.; Kumar, S.; Bozhevolnyi, S. I. Nanofabrication of Plasmonic Circuits Containing Single Photon Sources. *ACS Photonics* **2017**, *4*, 1879−1884.
(60) Passaro, V.; Tullio, C. D.; Troia, B.; Notte, M. L.; Giannoccaro, G.; Leonardis, F. D. Recent Advances in Integrated Photonic Sensors. *Sensors* **2012**, *12*, 15558−15598.

https://dx.doi.org/10.1021/acsnano.0c04301
ACS Nano 2020, 14, 10428−10437